Check for updates

Solar RRL
www.solar-rrl.com

Engineering the Core Units of Small-Molecule Acceptors to Enhance the Performance of Organic Photovoltaics

*Hao-Cheng Wang, Chung-Hao Chen, Ren-Hao Li, Yu-Che Lin, Cheng-Si Tsao, Bin Chang, Shaun Tan, Yang Yang, and Kung-Hwa Wei**

Understanding the chemical structures of next-generation small molecules is a critical step for increasing the performance of organic photovoltaics (OPVs); an OPV's small molecule determines not only the extent of light absorption but also the morphology. Herein, four small molecules featuring different cores—indaceno dithiophene, dithienoindeno indaceno dithiophene (IDTT), substituted IDTT, and dithienothiophene-pyrrolobenzothiadiazole—denoted as ID-4Cl, IT-4Cl, m-ITIC-OR-4Cl, and Y7, respectively, are selected to form active layers with poly(quinoxaline) (PTQ10) and poly(benzodithiophene-4,8-dione) (PM6). The Y7 devices exhibit the best performance in both systems, with the power conversion efficiency (PCE) reaching 14.5%; in comparison, ID-4Cl device gives a PCE of 10.0% for blending with PTQ10 and a relative efficiency enhancement of 45%. The same trend occurs for the cases of PM6 blend devices. This enhancement is attributed to i) the improved short-circuit current density that is provided by the greater degree of conjugation in S, N-heteroarenes ladder-type fused-ring cores of Y7, ii) an induced face-on Y7 orientation and smaller domain sizes that result from the sp^2-hybridized nitrogen side chain, and iii) smaller energy loss. This study reveals the importance of the core structure on the device performance and provides guidelines for the design of new materials for OPV technologies.

1. Introduction

Organic photovoltaics (OPV) is a rapidly emerging next-generation technology[1,2] because of its light weight, flexibility, compatibility with large-area fabrication, transparency, and potentially low cost.[3] Currently, bulk heterojunction (BHJ) structures are the most prevalent and effective active-layer designs for OPVs; they typically comprise nanometer-scale phase-separated blends of donor and acceptor (p- and n-type) materials that form large interfacial contact areas and many pathways for carrier transport.[4] OPVs have experienced rapid development, with their power conversion efficiencies (PCEs) recently surpassing 17% for single-junction devices.[5] The BHJ active layer morphology is affected by the relative molecular packing of the donor and acceptor[6] and, furthermore, can have a critical effect on OPV performance. The BHJ morphology can be optimized by, for example, tuning the donor-to-acceptor ratio, changing the molecular weight, and controlling the processing parameters during fabrication (e.g., annealing temperature, solvent, annealing of the solvent, or use of solvent additives).[7] Many strategies to improve BHJ film morphologies have involved modifying the molecular structure of non-fullerene acceptors (NFAs) to match the energy levels of the donors.[8]

In recent years, remarkable developments in the design and synthesis of novel NFAs have led to dramatic increases in achievable PCEs.[9] Tailoring the chemical structure of an NFA to that of the polymer donor can lead to an active layer capable of harvesting photons over a broader range and improving carrier transport; the relative ease of modifying the structures of NFAs provides a wealth of potential materials for achieving high-efficiency OPVs.[10] The development of low-band-gap NFAs with acceptor–donor–acceptor (A–D–A) structures has been advanced extensively; for example IT-4F consists of IDTT core and fluorine atoms in the end-capping show promising device efficiency.[10a] Furthermore, introducing the nitrogen atoms form S,N-heteroarene ladder-type fused ring cores and replacing sp^3 carbon with sp^2

H.-C. Wang, C.-H. Chen, R.-H. Li, Dr. Y.-C. Lin, B. Chang, Prof. K.-H. Wei
Department of Materials Science and Engineering
National Chiao Tung University
Hsinchu 30010, Taiwan
E-mail: khwei@mail.nctu.edu.tw

Prof. C.-S. Tsao
Department of Materials Science and Engineering
National Taiwan University
Taipei 10617, Taiwan

The ORCID identification number(s) for the author(s) of this article can be found under https://doi.org/10.1002/solr.202000253.

DOI: 10.1002/solr.202000253

Prof. C.-S. Tsao
Institute of Nuclear Energy Research
Taoyuan 32546, Taiwan

S. Tan, Prof. Y. Yang
Department of Material Science and Engineering
University of California
Los Angeles, CA 90095, USA

Prof. K.-H. Wei
Center for Emergent Functional Matter Science
National Chiao Tung University
Hsinchu 30010, Taiwan

 © 2020 Wiley-VCH GmbH

nitrogen units of A–D–A-structured small-molecule acceptors often enhance their possibility to undergo intramolecular charge transfer (ICT) as well as alter their packing orientation.[11] In this vein, chlorination of the conjugated backbone might be preferable because it is inexpensive, synthetically simple, and higher yielding.[12] At present, the two main methods to promote charge transport, by accelerating charge dissociation and decreasing charge density at the contact interface, involve 1) extending the fused-ring conjugated system to enhance the electron-donating ability and 2) adding a strong electron-withdrawing group at both ends of the fused ring core to promote electron delocalization.[13] Several studies have demonstrated the suitability of using poly(thiophene–quinoxaline) (PTQ) derivatives as inexpensive D–A copolymer donors (e.g., PTQ10), featuring either one or two fluorine atoms substituted on their quinoxaline (Qx) acceptor units.[14] At present, a widely used conceptual framework for determining the best-matched acceptor material for a given donor polymer is to carefully consider the influences of each factor individually.[15] Nevertheless, the many variables make it extremely challenging to predict the optimal BHJ morphology and performance of an OPV when designing or using new materials.[16] Varying the acceptor core unit is one way to tune the molecular aggregation, solubility, optical absorption, and intermolecular interactions of BHJ layers.

In this study, we prepared binary blend active layers for OPV devices using four small-molecule acceptors, featuring the same chlorinated end-capping units but different core units along with different side chain positions and two polymer donors. We investigated the effects of the core units on the packing arrangement, crystallinity, and morphology of the active layers and the resulting photovoltaic performance of OPVs. Our four small molecules featured the following core units: 1) ID-4Cl, a 4,9-dihydro-*s*-indaceno[1,2-*b*:5,6-*b*′]dithiophene (IDT) fused-ring core (a smaller fused-ring core than that in ITIC);[17] 2) IT-4Cl, a 6,12-dihydrodithienoindeno[2,3-*d*:2′,3′-*d*′]-*s*-indaceno [1,2-*b*:5,6-*b*′]dithiophene (IDTT) fused-ring core; 3) m-ITIC-OR-4Cl, an IDTT fused-ring core with side chain isomerization with *meta*-oxyalkylphenyl substitution;[18] and 4) Y7, S, N-heteroarenes ladder-type pyrrole, a dithienothiophen[3.2-*b*]-pyrrolobenzothiadiazole (TPBT) fused-ring core.[19] For the donors, we chose PTQ10, a commercially available polymer that exhibits complementary absorption and features a large band gap, having a lowest unoccupied molecular orbital (LUMO) energy level of –2.98 eV and a highest occupied molecular orbital (HOMO) energy level of –5.54 eV and PM6 that has been one of the best donor systems and its energy levels can be found in a previous study.[19] The structure of the IDT and IDTT core unit has an sp^3-hybridized carbon side chain that is different from Y7 where TPBT has S, N-heteroarenes ladder-type pyrrole fused ring and sp^2-hybridized nitrogen side chain, and thus Y7 has significantly better miscibility than ID-4Cl, IT-4Cl, and m-ITIC-OR-4Cl with PTQ10, resulting in higher PCEs for the Y7 photovoltaic devices. In particular, the core units determined the arrangement and orientation of the small molecules in the active layers formed with PTQ10. We obtained a PCE as high as 14.5% for the optimized device incorporating PTQ10:Y7. This strategy for improving the performance of OPVs would appear to be suitable for the fabrication of other electronic devices based on polymer/NFAs blends.

2. Results and Discussion

2.1. Chemical Structures and Optical Properties

Figure 1 shows the chemical structures of the small molecules ID-4Cl, IT-4Cl, m-ITIC-OR-4Cl, and Y7 and of the polymer PTQ10. **Figure 2**a shows the device configuration used for each of the four cases. Figure 2b shows that Y7 has a lower LUMO energy level, but a higher HOMO energy level, than those of the other three acceptors. The higher HOMO energy level of Y7 implies enhanced π-electron delocalization in the charge-deficient fused-ring core region, consistent with its red-shifted absorption and lower bandgap.[20] When designing NFAs for efficient BHJ solar cells, the π-electron delocalization, backbone planarity, and spectral absorption are all crucial factors for consideration. We used density functional theory (DFT) to identify possible candidates having electron-rich units with high HOMO levels, rigid backbone structures, and possible modification sites. Figure 2c shows the DFT-calculated core structures of the four

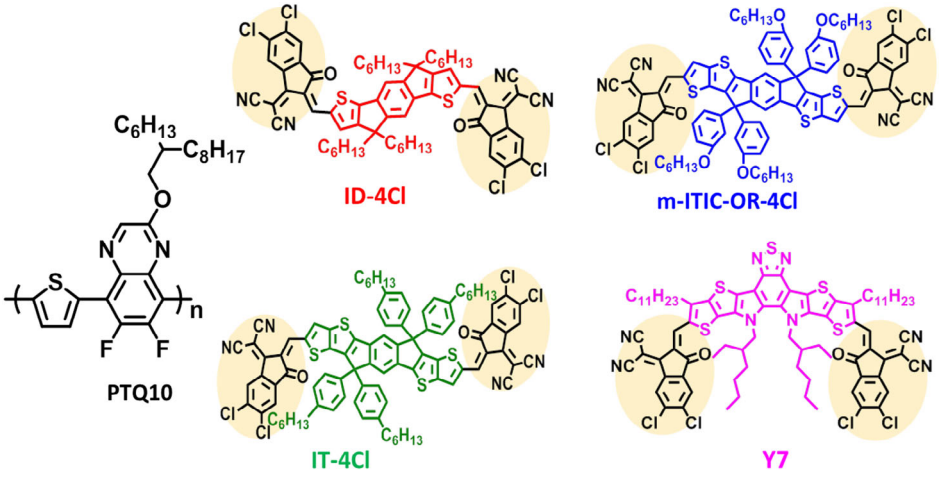

Figure 1. Chemical structures of the small-molecule acceptors ID-4Cl, IT-4Cl, m-ITIC-OR-4Cl, and Y7, and the polymer PTQ10.

© 2020 Wiley-VCH GmbH

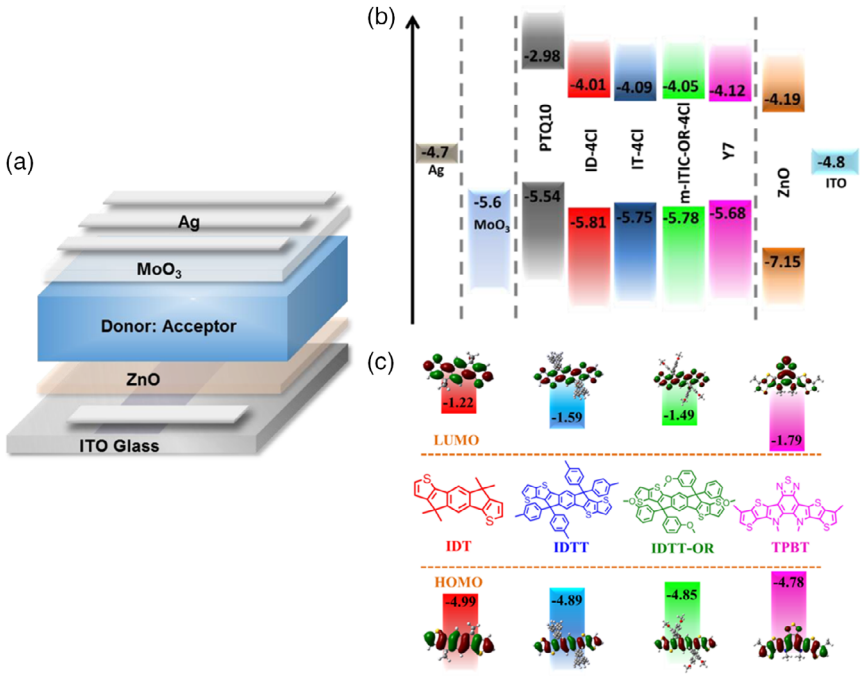

Figure 2. a) Device architecture of the nonfullerene OPVs. b) Energy levels of the materials. c) Energy levels of the cores, calculated using DFT.

small molecules having IDT, IDTT, and TPBT cores and the same chlorinated end-capping groups.

Figure 2b,c shows the calculated HOMO and LUMO energies (determined using DFT at the B3LYP/6-31 G** level) for the NFA core units, as well as the whole molecules' experimental values (determined using cyclic voltammetry [CV]). The calculated HOMO/LUMO energy levels were –4.99/–1.22 eV for IDT, –4.89/–1.59 eV and –4.85/–1.49 eV for IDTT, and –4.78/–1.79 eV for TPBT. For IDTT, the larger fused-ring core region, relative to that of IDT, helps to improve its electron-donating ability. For TPBT, a broadened central core unit and 2D conjugation, incorporating strongly electron-donating nitrogen heteroatoms, further increased the energy levels and red-shifted the absorption of the ICT; the nitrogen atoms were also possible modification sites on the molecular backbone.[21] The TPBT core unit allows electrons to effectively delocalize along its large ring, while also displaying significantly improved chemical stability.[19] Acceptors featuring extended conjugation and highly planar backbone structures generally facilitate π-stacking of the resulting NFAs.[22] As a result, Y7 had the smallest optical band gap (1.56 eV) among these four NFAs. Using a complementary light-absorbing polymer donor PTQ10, we showed that PTQ10:Y7-based devices demonstrated a high PCE up to 14.5% and an extremely low energy loss of 0.51 eV.

We made some further modifications to adjust the chemical structures and energy levels. Figure 2b shows the DFT data with the experimental measurements. The chlorinated end-capping units on the side chains did not significantly affect the conformations of the conjugated backbones, but their presence did slightly decrease the HOMO energy levels.

Figure 3 shows the UV–vis absorption spectra of films of the small molecules ID-4Cl, IT-4Cl, m-ITIC-OR-4Cl, and Y7. The absorption maximum peak of Y7 film red-shifted to 828 nm from 730 nm from the solution state (Figure S1a, Supporting Information), presumably because of the induced aggregation of the molecules by the alkyl chains on the pyrrole and thienothiophene units in its TPBT core. Figure 3b shows that the absorption coefficient (ε) of the PTQ10:Y7 blend film at 600 nm (5.8×10^4 cm^{-1}) was higher than those of the other three binary blend films (for PTQ10:ID-4Cl, PTQ10:IT-4Cl, and PTQ10:m-ITIC-OR-4Cl: 5.6×10^4, 4.3×10^4, and 5.6×10^4 cm^{-1}, respectively). The optical band gaps (E_g^{opt}) of ID-4Cl, IT-4Cl, m-ITIC-OR-4Cl, and Y7 were 1.51, 1.48, 1.50, and 1.34 eV, respectively (Figure 3a). Therefore, the electrochemical and optical data demonstrated that small molecules having ladder-type multifused rings and an electron-deficient core as the central unit had very narrow band gaps. Both a red-shifted signal in the absorption spectrum and a higher absorption coefficient would enhance an acceptor core unit's suitability for improving the optoelectronic properties of resulting devices. The much broader optical absorption range and higher absorption coefficient of the PTQ10:Y7 film, relative to those of the other three blend films, would be beneficial for photon harvesting. Notably, the broader absorption of Y7, with its electron-poor units (TPBT) and D–A–D-structured fused core unit, exhibited a stronger ICT effect, relative to those of IDT or IDTT cores, potentially enhancing the short-circuit current densities (J_{SC}) of its OPV devices.

2.2. Photovoltaic Performance

Figure 4a,b shows the J–V and external quantum efficiency (EQE) curves, respectively, of the OPVs. **Table 1** shows the photovoltaic parameters. The champion device incorporating

© 2020 Wiley-VCH GmbH

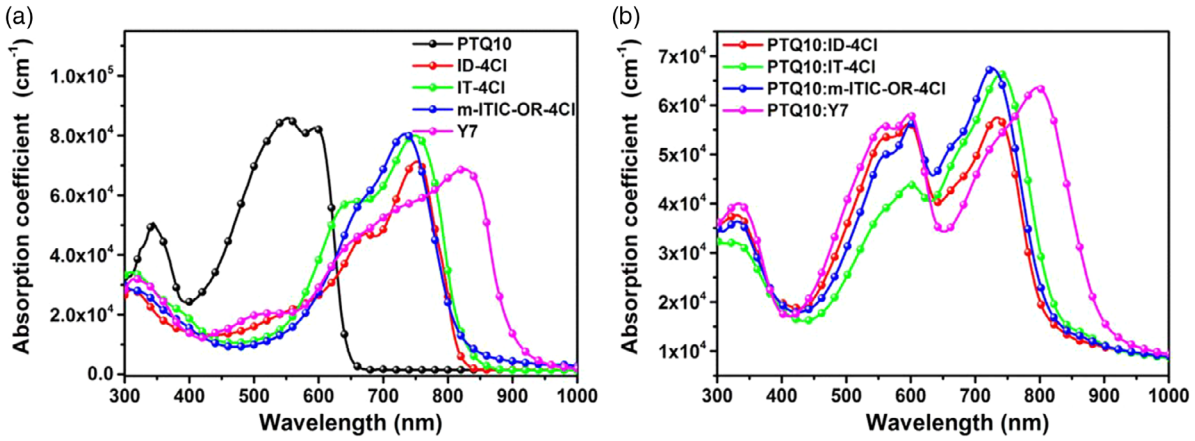

Figure 3. UV–vis absorption spectra of a) the individual materials and b) the binary blend films.

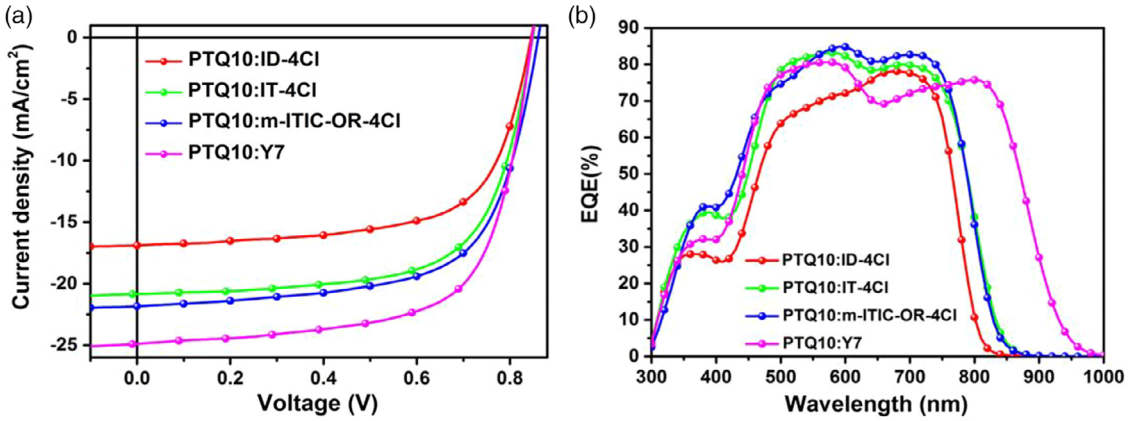

Figure 4. a) *J–V* characteristics and b) EQE curves of devices incorporating the four different binary blends.

Table 1. Photovoltaic parameters of OPV devices incorporating the four different binary blends.

Active layer	V_{OC} [V]	J_{SC} [mA cm^{-2}]	$J_{SC,\ cal}$ [mA cm^{-2}]	FF [%]	PCE_{avg} [%][a)]	PCE_{max} [%]
PTQ10:ID-4Cl	0.85 ± 0.01	17.3 ± 0.2	16.7	65.5 ± 0.4	9.5 ± 0.1	10.0
PTQ10:IT-4Cl	0.85 ± 0.01	21.2 ± 0.2	20.3	66.4 ± 0.5	11.9 ± 0.2	12.2
PTQ10:m-ITIC-OR-4Cl	0.87 ± 0.01	21.8 ± 0.2	20.7	66.9 ± 0.3	12.6 ± 0.1	12.7
PTQ10:Y7	0.85 ± 0.01	24.1 ± 0.2	23.5	69.1 ± 0.5	14.2 ± 0.2	14.5

[a)]Twenty devices were fabricated in each case.

the PTQ10:Y7 blend as the active layer displayed a value of V_{OC} of 0.85 V, a value of J_{SC} of 24.1 mA cm^{-2}, and a fill factor (FF) of 69.1%, resulting in a PCE of 14.5%. The open-circuit voltages of the devices based on PTQ10:IT-4Cl and PTQ10:m-ITIC-OR-4Cl were 0.85 and 0.87 V, respectively. As indicated in the energy-level diagram in Figure 2b, the higher value of V_{OC} of the PTQ10:m-ITIC-OR-4Cl blend, relative to that of the PTQ10:IT-4Cl blend, was consistent with its deeper HOMO and higher LUMO energy levels. From the absorption onset data (Figure 3b), the optical bandgaps of the PTQ10:ID-4Cl, PTQ10:IT-4Cl, PTQ10:m-ITIC-OR-4Cl, and PTQ10:Y7 blends were 1.50, 1.47, 1.48, and 1.36 eV, respectively; these values result in energy losses of 0.65, 0.62, 0.61, and 0.51 eV, respectively.[23] The much smaller loss in the open-circuit voltage of Y7 is consistent with its very narrow bandgap.[22]

The short-circuit current density (J_{SC}) was the primary factor affecting the performance of our devices incorporating the four different binary blends. The PTQ10:Y7 device gave the highest value of J_{SC} of 24.1 mA cm^{-2} because of the more complementary absorption of PTQ10 and Y7. The integrated photocurrents for the devices based on pristine PTQ10:ID-4Cl, PTQ10:IT-4Cl, PTQ10:m-ITIC-OR-4Cl, and PTQ10:Y7 were 16.7, 20.3, 20.7,

© 2020 Wiley-VCH GmbH

and 23.5 mA cm^{-2}, respectively. The EQE spectrum of the PTQ10:Y7 blend revealed enhanced photon harvesting and conversion from 800 to 950 nm. The measured values of J_{SC} of the devices were consistent with those calculated by integrating their EQE curves, with deviations in the range from 2.5% to 4.5%, confirming the reliability of our test results. The FFs of our OPVs varied to some extent, ranging from 65.5% to 69.1%, suggesting that the planarity of the core unit affected the blend morphology through aggregation effects.

2.3. Morphological Characterization

We undertook a mechanistic study to determine how the morphology—in particular, the phase separation—of the BHJ active layer was affected by the molecular structure of the acceptors and could be correlated with the OPV performance data.[24] We used grazing-incidence small-angle X-ray scattering (GISAXS) to quantitatively probe the BHJ structure of the blend films at multiple length scales.[25] We used grazing-incidence wide-angle X-ray scattering (GIWAXS) to investigate the crystal structure, crystallinity, and orientation of each polymer donor/small-molecule acceptor blend. **Figure 5**a shows the 2D GIWAXS patterns of the PTQ10:Y7, PTQ10:ID-4Cl, PTQ10:IT-4Cl, and PTQ10:m-ITIC-OR-4Cl blend films. Figure 5b,c shows the 1D in-plane and out-of-plane GIWAXS profiles of the individual pristine films and blend films. In Figure 5b, the GIWAXS pattern of the pristine PTQ10 polymer featured a main (100) peak at a value of q_z of 0.27 Å^{-1} in the out-of-plane direction, indicating a lamellar structure with a spacing of 23.26 Å between the (100) planes. The main lamellar crystallites had mainly an edge-on orientation with minor face-on crystallites. The main crystallites in the pristine Y7 film had a face-on orientation with minor edge-on crystallites. Figure 5b also shows that the (100) and (010) peaks of the Y7 crystallites were located at values of q of 0.32 and 1.80 Å^{-1}, respectively, in the in-plane and out-of-plane directions. The spacing between the (100) planes of the corresponding Y7 crystallites was 19.6 Å. The pristine m-ITIC-OR-4Cl, IT-4Cl, and ID-4Cl films had crystallites in an edge-on orientation.

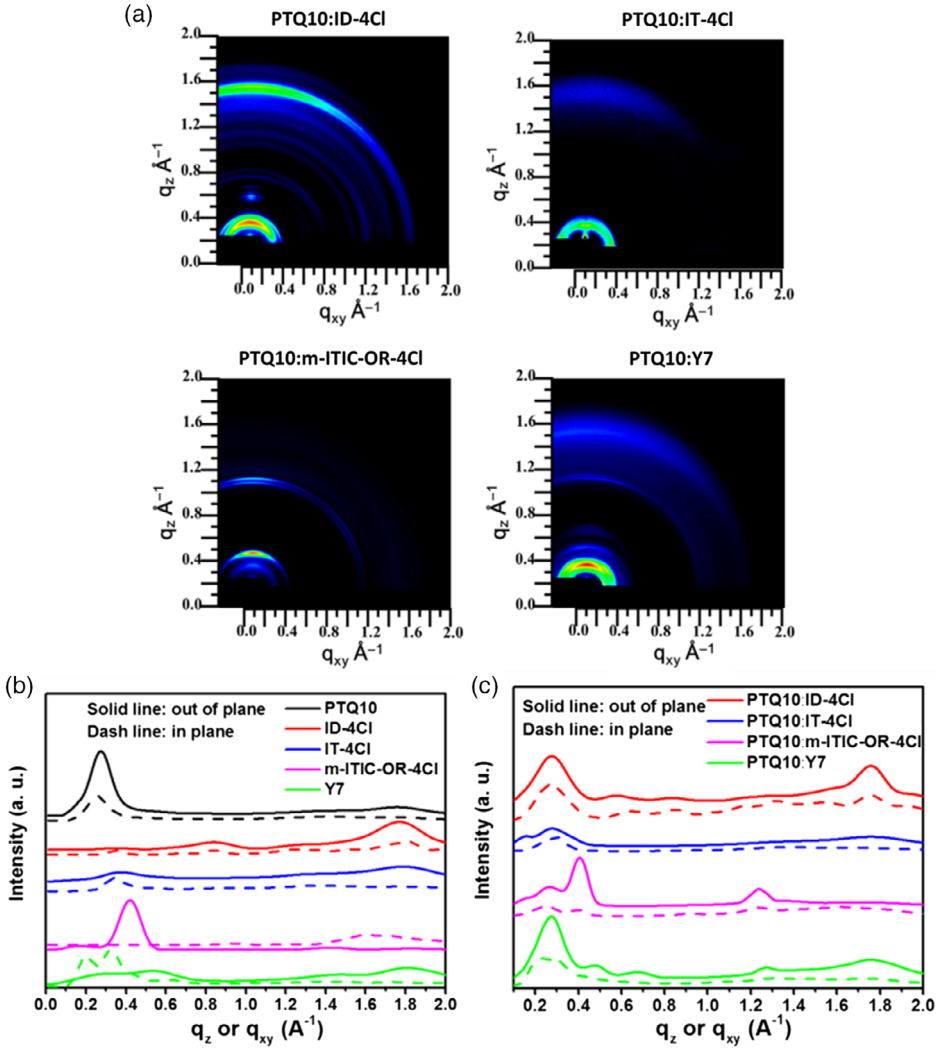

Figure 5. a) 2D GIWAXS patterns of the binary blend films PTQ10:ID-4Cl, PTQ10:IT-4Cl, PTQ10:m-ITIC-OR-4Cl, and PTQ10:Y7. b,c) Corresponding 1D GIWAXS profiles of b) the individual films and c) the binary blend films, reduced from the in-plane and out-of-plane directions.

© 2020 Wiley-VCH GmbH

The (100) peaks of the m-ITIC-OR-4Cl, IT-4Cl, and ID-4Cl crystallites appeared at 0.42, 0.37, and 0.35 $Å^{-1}$, respectively; the corresponding spaces between the (100) planes were 14.9, 16.9, and 17.9 Å, respectively. The relative crystallinity of the PTQ10 crystallites in the blend films with each of the different acceptor molecules could be determined from the intensity of the (100) peak. Based on Figure 5c, we concluded that the relative crystallinities of the PTQ10 crystallites in the blend films with the acceptors Y7 and ID-4Cl were much higher than those of the blend films with IT-4Cl and m-ITIC-OR-4Cl, suggesting that IT-4Cl and m-ITIC-OR-4Cl were dispersed relatively well in the blend films, due to their more suitable molecular structures, and, thus, they hindered the crystallization of PTQ10. The crystallinities (or peak intensities) of the IT-4Cl and m-ITIC-OR-4Cl acceptor phases in the blend films (Figure 5c) were relatively weak, indicating that these acceptors were more highly dispersed in the amorphous matrices.

Figure 6a shows the 1D GISAXS profiles in the low-q region (<0.01 $Å^{-1}$) of the pristine PTQ10 film, revealing power-law scattering behavior [$I(q) \propto q^{-n}$; $n \approx 1$] with an exponent of –1, indicating that PTQ10 formed rod-like domains in the amorphous film. In contrast, the GISAXS profiles in the low-q region (<0.02 $Å^{-1}$) of the pristine ID-4Cl, IT-4Cl, m-ITIC-OR-4Cl, and Y7 films revealed power-law scattering behavior with an exponent of ≈–2, characteristic of disk-like domains. Based on SAXS theory, exponents of –1 and –2 are characteristic of rod- and disk-like domains, respectively.[26] Figure 6b shows the 1D GISAXS profiles of the PTQ10:Y7, PTQ10:ID-4Cl, PTQ10:m-ITIC-OR-4Cl, and PTQ10:IT-4Cl blend films. In the low-q region, the GISAXS profiles of these blend films exhibited power-law scattering at the exponent of –2 or slightly lower, indicative of a disk-like morphology for the acceptor domains being the dominant contributor to the GISAXS intensity.[27] On the other hand, the middle-q region (0.01 $Å^{-1} < q < 0.04$ $Å^{-1}$) of the GISAXS profile of the PTQ10:m-ITIC-OR-4Cl blend film featured a power-law scattering with an exponent of –1, mainly contributed by the rod-like PTQ10 domain. The long-rod morphology of the PTQ10 crystalline domains would be similar to the long-fiber morphologies of the well-established P3HT and BO2S crystallites formed by long-chain packing.[27b] The disk-like morphologies of the four acceptor domains might have been due to favorable aggregation of the acceptor molecules into 2D-like architectures.[27] GISAXS intensities contributed by the PTQ10 polymer and the various crystalline acceptor domains could be modeled simultaneously in terms of the sum of the form factors, with the rod-like particles contributing in the middle-q region and the disk-like particles contributing mainly in the low-q region. The form factor of polydisperse cylinders having a radius R and a mean thickness T, with Schulz distribution in thickness, mainly contributing in the low-q region and describing the disk-like acceptor domains, can be expressed as follows.

$$I(Q) = \frac{\eta}{(V_P)} \cdot \Delta\rho^2 \cdot \int_0^x \int_0^{\frac{\pi}{2}} \left[2(\pi R^2 t) f(r) j_0\left(\frac{Qt}{2}\cos\alpha\right) \frac{j_1(QR\sin\alpha)}{(QR\sin\alpha)} \right]^2 \sin\alpha \, d\alpha dr \quad (1)$$

where η is the volume fraction of the disk domains, $\Delta\rho$ is the difference in the scattering length densities between the domains and the amorphous matrix (formed by intermixing of the donor and acceptor molecules), $f(r)$ is the Schulz distribution of the thickness, V_P is the mean volume of polydisperse domains, and j_0 and j_1 are the spherical Bessel functions of the zero and first order. The polydispersity p of the Schulz distribution is related to the variance of distribution. The integral over α is the average of the form factors with all orientations with respect to q. The product of η and $\Delta\rho$ can be regarded as a prefactor during the least-squares calculation of model fitting. The other form factor describing the rod-like domains and contributing in the middle-q region can be expressed by the simple cylinder form factor, as in Equation (1), but without considering Schulz distribution, with the length greater than the radius. Note that the fitted radius of disk-like domains was based on the extrapolation of fitting toward the low-q region beyond measurement, providing large uncertainties.

Figure 6b shows that the GISAXS profiles of all of the blend films could be fitted well by the model (solid lines). Based on the fitting data, the rod-like PTQ10 crystalline domains in the four blend films all had different radii, causing the disk-like acceptor domains to form with various sizes, due to the mutual confinement effect during film formation. The fitted radii of the long-rod PTQ10 domains in the blend films with Y7, IT-4Cl, m-ITIC-OR-4Cl,

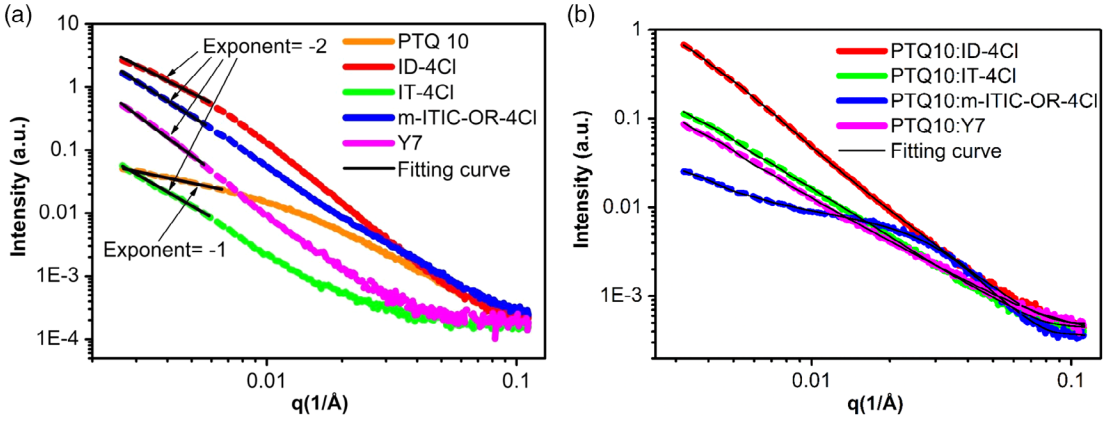

Figure 6. 1D GISAXS profiles of a) pure films (power-law scattering region marked by solid black lines) and b) binary blend films (with model-fitted intensities [solid black lines]).

© 2020 Wiley-VCH GmbH

and ID-4Cl were 2, 3, 4, and 12 nm, respectively. The determined polydispersity of the radii was ≈0.3. The fitted radii/thicknesses of the Y7, IT-4Cl, m-ITIC-OR-4Cl, and ID-4Cl domains in the blend films were 125/9, 125/15, 146/2.5, and 170/5 nm, respectively. Thus, in these four systems, the radius of the PTQ10 rod domains in the Y7 blend film was the shortest, whereas that in the ID-4Cl blend film was the longest. Consistently, the radii of the Y7 and ID-4Cl disk domains were similar. We conclude that the PTQ10:Y7 film had the largest interfacial area between the donor and acceptor, whereas the PTQ10:ID-4Cl film had the lowest. A larger interfacial area favors charge separation, enhancing the values of J_{SC} and PCE. This finding explains the different values of J_{SC} and PCE we obtained for the OPVs incorporating different blend films. In addition, charge separation is closely related to recombination dynamics, suggesting another reason as to why the PTQ10:Y7 and PTQ10:ID-4Cl films had highest and lowest hole mobilities, respectively. Although the polymer in the PTQ10:ID-4Cl blend film had excellent crystallinity, the low interfacial area affected its performance. In conclusion, we attribute the high performance of the PTQ10:Y7 blend film to 1) the high crystallinity PTQ10 polymer (generating more excitons) and 2) the large interfacial (facilitating effective charge separation) region. To illustrate our findings from the structural characterizations made using GISAXS and GIWAXS, **Figure 7** shows schematic representations of the BHJ structures formed from PTQ10 and the four different NFAs. **Table 2** shows the results.

We used a tapping-mode atomic force microscope (AFM) to examine the effects of the four core units on their film morphologies (Figure S3, Supporting Information). The height images of the PTQ10:ID-4Cl, PTQ10:IT-4Cl, PTQ10:m-ITIC-OR-4Cl, and PTQ10:Y7 films provided root-mean-square (RMS) surface roughnesses of 2.56, 1.66, 1.59, and 1.51 nm, respectively. A smooth interfacial contact is ideal for increasing the contact area, facilitating interactions between the active layer and the interlayer and, thereby, achieving more efficient charge carrier extraction from the active layer to the anode.[28] We suspect that decreases in the RMS roughness occurred as a result of greater dispersion of the long-side-chain acceptors and better miscibility of the donor and acceptor; the latter can greatly influence the morphology of a blend film.[12b,29]

The DFT data in Figure S5, Supporting Information, reveal that the dihedral angles between the planes of the central core units and the chlorinated end-capping units followed the order m-ITIC-OR-4Cl (13.04°) > Y7 (6.23°) > ID-4Cl (2.15°) > IT-4Cl (2.02°); these differences affected the molecular packing of the NFAs and the polymer in the film state. Compared with m-ITIC-OR-4Cl and Y7, smaller dihedral angles were found in ID-4Cl and IT-4Cl, suggesting that these two NFAs had spiro-like cores that over-aggregated with the alkyl side chains.[27b] The DFT data also revealed that the planarity between the core units and the chlorinated end-capping units improved upon proceeding from m-ITIC-OR-4Cl to Y7. Thus, excessive aggregation and different domain sizes both affected the FFs significantly.

To better understand the miscibility between PTQ10 and the small-molecule acceptors, we measured the surface energies of the individual acceptors. Because the structure of the core unit was the only chemical difference between the acceptors, we speculated that the different morphologies of the blend films resulted from the different miscibilities of the polymer donor in the different acceptors.[30] We measured contact angles to estimate the surface energies of the corresponding films. Figure S6,

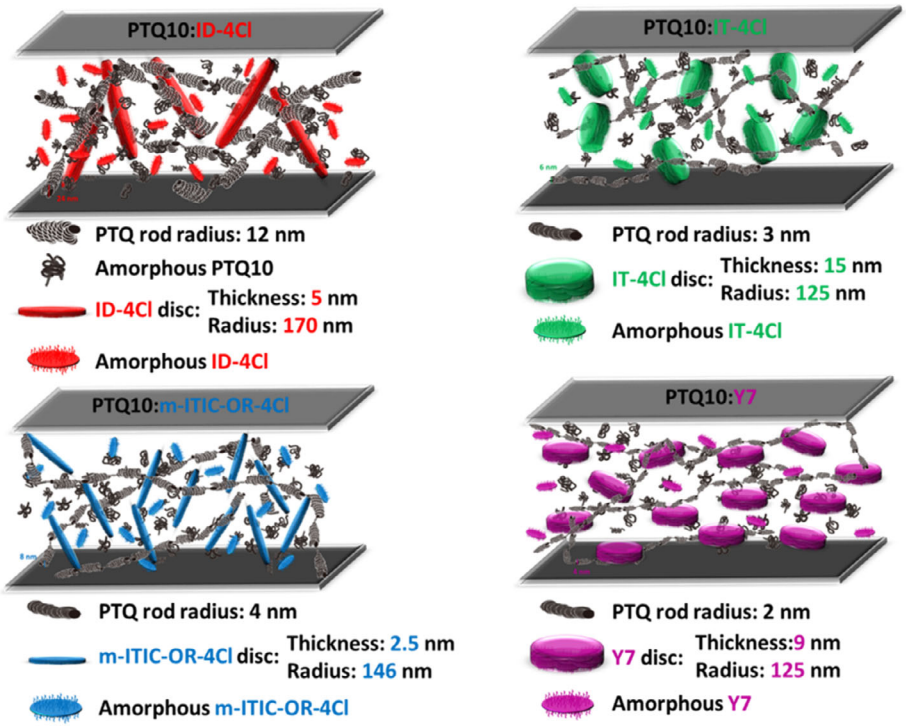

Figure 7. Schematic representations of possible BHJ structures for the four blend films.

© 2020 Wiley-VCH GmbH

Table 2. GIWAXS and GISAXS data of the pure and binary blend films.

	Pure	Binary					
		Crystallite orientation		Relative crystallinity of PTQ10	PTQ10 radius [nm]	Acceptor domain size	
		PTQ10	Acceptor			Radius [nm]	Thickness [nm]
PTQ10	Edge on						
ID-4Cl	Edge on	Edge on	Edge-on	medium	12	170	5
IT-4Cl	Edge on	Edge on	Edge on	lowest	3	125	15
m-ITIC-OR-4Cl	Edge on	Edge on	Edge on	medium	4	146	2.5
Y7	Face on	Edge on	Face on	highest	2	125	9

Table 3. Contact angles and surface tensions of the individual organic layers and values of $(\sqrt{\gamma \text{donor}} - \sqrt{\gamma \text{acceptor}})^2$ values.

Organic layer	Water contact angle [°]	1,2-ethanediol contact angle [°]	γ^d [mN m^{-1}]	γ^p [mN m^{-1}]	Surface energies [mN m^{-1}]	$(\sqrt{\gamma \text{donor}} - \sqrt{\gamma \text{acceptor}})^2$
PTQ10	101.1	67.8	2.47	28.42	30.90	
ID-4Cl	88.9	70.1	14.66	10.68	25.34	0.27
IT-4Cl	86.4	71.4	17.70	8.65	26.35	0.18
m-ITIC-OR-4Cl	95.4	66.3	6.99	19.63	26.63	0.15
Y7	81.5	66.6	20.02	9.26	29.28	0.02

Supporting Information, shows relevant images; **Table 3** shows the parameters. The surface energies of PTQ10, ID-4Cl, IT-4Cl, m-ITIC-OR-4Cl, and Y7 were 30.90, 25.34, 26.35, 26.63, and 29.28 mN m^{-1}, respectively. The value of the molecular interaction parameter χ or $(\sqrt{\gamma \text{donor}} - \sqrt{\gamma \text{acceptor}})^2$ reflects the binary miscibility, with a smaller value of χ indicating greater miscibility.[12b] In this case, the smallest $(\sqrt{\gamma \text{donor}} - \sqrt{\gamma \text{acceptor}})^2$ value of χ was that for Y7, indicating that the PTQ10:Y7 blend had the best miscibility among our tested systems. Better miscibility would lead to more intimately mixed blends and lower degrees of phase separation. The data suggest that Y7, with its alkyl chains on the pyrrole ring and thienothiophene for the TPBT core, modulating the miscibility of the two components in the active layer, formed a proper BHJ morphology—a prerequisite to ensure that high-dielectric-constant materials would be useful in OPVs in practice.[30] Decreasing the surface energy of the polymer donor, to generate an appropriate difference in surface energies between the polymer donor and acceptor would be a feasible approach to adjust the BHJ morphology; it would also potentially improve the interfacial contact between the transport layers and the active layer, leading to larger PCEs. An ideal interface would most likely feature fewer traps, thereby decreasing the probability of recombination.[31]

2.4. Charge Transport and Charge Recombination

To investigate the effects of the core units on exciton generation, we measured the photoluminescence (PL) spectra of our four PTQ10:acceptor blends. Figure S7, Supporting Information, reveals that PTQ10 (excited at 580 nm) exhibited a broad PL peak from ≈710 to 870 nm. The signals in the PL spectra of the binary blends were substantially quenched. The acceptors having long side chains and planar ladder-type multifused rings as their core units exhibited a much stronger PL quenching—from 77.8% for ID-4Cl to 88.9%, 94.5%, and 97.3% for IT-4Cl, m-ITIC-OR-4Cl, and Y7, respectively. Nevertheless, the film of the PTQ10:ID-4Cl blend displayed a strong emission, indicative of a low charge-transfer efficiency. In contrast, for the PTQ10:Y7 blend film, the PL peak was nearly fully quenched, indicating enhanced exciton dissociation and charge transfer.

We used the space charge limited current (SCLC) method to evaluate the charge carrier mobility of the BHJ photoactive layers (Figures S9a,b, Supporting Information). We calculated the electron (μ_e) and hole (μ_h) mobilities based on the Mott–Gurney equation.[32]

$$J_{\text{SCLC}} = \frac{9}{8}\varepsilon_r \varepsilon_0 \mu \frac{V^2}{d^3} \tag{2}$$

where J_{SCLC} is the current density; ε_0 and ε_r are vacuum dielectric permittivity and relative dielectric permittivity, respectively; d is the thickness of the blend film; V is the applied voltage; and μ is the charge carrier mobility, calculated from the fitting curve.

The hole mobilities for the devices based on PTQ10:ID-4Cl, PTQ10:IT-4Cl, PTQ10:m-ITIC-OR-4Cl, and PTQ10:Y7 were 1.6×10^{-4}, 2.5×10^{-4}, 7.6×10^{-4}, and 1.5×10^{-3} cm^2 V^{-1} s^{-1}, respectively; their electron mobilities were 4.7×10^{-5}, 8.1×10^{-5}, 3.4×10^{-4}, and 8.2×10^{-4} cm^2 V^{-1} s^{-1}, respectively. The slightly higher electron mobility in the neat PTQ10:Y7 film can be explained by the replacement of the sp^3-hybridized carbon atoms in the IDT and IDTT cores with the nitrogen atoms of pyrrole rings in Y7 as well as its higher crystallinity relative to the other small molecules in the blend films, particularly the case of PTQ10:ID-4Cl, as evidenced in the GIWAXS and AFM data. The μ_h/μ_e ratio was best balanced (1.8) for the PTQ10:Y7 device, implying not only a higher degree of charge transport but also more balanced mobility and, thus, a superior morphology; accordingly, this device exhibited the highest PCE (14.5%)

© 2020 Wiley-VCH GmbH

among our tested devices. The observed higher and more balanced charge carrier mobility of the PTQ10:Y7 film correlates with its higher FF (69.1%); the much lower and less balanced charge carrier mobility of the PTQ10:ID-4Cl film is consistent with the much lower FF (65.5%) of its corresponding OPV (Table 1). A balanced μ_h/μ_e ratio is generally due to a more suitable and coordinating blend aggregation behavior, conducive to a high FF.[33]

The μ_h/μ_e ratio can be considered as a measure of charge accumulation in a device. Imbalanced carrier mobility can lead to positive space–charge build-up at the photoanode and, therefore, the trapping of electrons near the back electrode in a BHJ OPV.[34] Our devices provided dramatically different μ_h/μ_e ratios: from 3.4 for the PTQ10:ID-4Cl device (see **Table 4**) to 1.8 for the PTQ10:Y7 device. This variation is significant because electron transport is considered a limiting factor for photocurrent generation in devices; it is determined by the charge carrier having the lowest mobility.[35] A higher value of μ_e in an OPV device would minimize exciton recombination in the active layer and, thus, increase the achievable FF. In addition to balanced charge mobility, the FF is also closely correlated to the bimolecular recombination rate in BHJ films.[36] Furthermore, balanced charge carrier mobilities in the devices would minimize the charge accumulation effect, consistent with the greater value of J_{SC} for the PTQ10:Y7 BHJ OPV.

Table 4. Hole and electron mobilities, and their ratios, in the OPV devices.

Device μ [cm^2 V^{-1} s^{-1}]	μ_h	μ_e	μ_h/μ_e
PTQ10:ID-4Cl	1.6×10^{-4}	4.7×10^{-5}	3.4
PTQ10:IT-4Cl	2.5×10^{-4}	8.1×10^{-5}	3.1
PTQ10:m-ITIC-OR-4Cl	7.6×10^{-4}	3.4×10^{-4}	2.2
PTQ10:Y7	1.5×10^{-3}	8.2×10^{-4}	1.8

Owing to the high-efficiency-polymer PM6 devices, we also measured the ID-4Cl, IT-4Cl, m-ITIC-OR-4Cl, and Y7 with PM6 binary blend devices; we summarized the devices' efficiencies in Table S1, Supporting Information, along with their *J*–*V* characteristics in Figure S10, Supporting Information. We found the same trend in the device efficiencies of PM6 and PTQ10 binary blends with the highest device efficiencies occurring in the PM6:Y7 and PTQ10:Y7 devices, respectively, as compared with that of the devices involving ID-4Cl, IT-4Cl, and m-ITIC-OR-4Cl.

Table 5 shows different reasons as to why the photovoltaic parameters of Y7 case were enhanced, as compared with those of other small-molecule cases.

First, the improved short-circuit current density displayed in the case of c-typed Y7 acceptor device, as compared with the cases of linear A–D–A-type acceptors—ID-4Cl, IT-4Cl, and m-ITIC-OR-4Cl—can be attributed to (i) the greater degree of conjugation in the symmetrical ladder-type fused-ring core structure, generating a stronger ICT effect in Y7 that provides broader light absorption because of electron-poor units (TPBT) and D–A–D-structured fused core units and (ii) induced face-on orientation and smaller domain sizes for the case of Y7, as compared with edge-on orientation for ID-4Cl, IT-4Cl, and m-ITIC-OR-4Cl where a disk-like morphology for the acceptor domains appears. Furthermore, the more balanced charge-carrier mobilities in the devices would minimize the charge accumulation effect, being consistent with the greater value of J_{SC} for the PTQ10:Y7 and PM6:Y7 devices.

Second, the FFs of the OPVs varied from 69.1 to 75.0% with Y7 case having the highest value, implying that the planarity of the core units also affected their packing in the blends.

Third, from the absorption onset data, the optical bandgaps of the PTQ10:ID-4Cl, PTQ10:IT-4Cl, PTQ10:m-ITIC-OR-4Cl, and PTQ10:Y7 blends were 1.50, 1.47, 1.48, and 1.36 eV, respectively; these values result in energy losses of 0.65, 0.62, 0.61, and

Table 5. Summary of the molecular structure and photovoltaic parameters of PTQ10 with small-molecule device.

		ID-4Cl	IT-4Cl	m-ITIC-OR-4Cl	Y7
Molecular structure		1) Linear A–D–A typed 2) sp^3 hybrided carbon atoms of cores unit 3) Weak ICT effects			1) c-typed (ladder typed) 2) Pyrrole rings fused core unit 3) Strong ICT effects
Short-circuit current density (J_{SC})					
Optical bandgaps (eV)		1.51	1.48	1.50	1.34
Mobility (cm^2 V^{-1} s^{-1})	Hole	1.6×10^{-4}	2.5×10^{-4}	7.6×10^{-4}	1.5×10^{-3}
	Electron	4.7×10^{-5}	8.1×10^{-5}	3.4×10^{-4}	8.2×10^{-4}
μ_h/μ_e ratio		3.4	3.1	2.2	1.8
FF					
RMS [nm]		2.56	1.66	1.59	1.51
Packing orientation		Edge on	Edge on	Edge on	Face on
Relative crystallinity of donor		medium	lowest	medium	highest
Acceptor domain size	Radius [nm]	12	3	4	2
	Thickness [nm]	5	15	2.5	9
Energy loss [eV]		0.65	0.62	0.61	0.51
Best efficiency [%]		10.0	12.2	12.7	14.5

© 2020 Wiley-VCH GmbH

0.51 eV, respectively, for their devices. The much smaller loss in the open-circuit voltage of Y7 device is consistent with its narrower bandgap, as compared with other cases.

3. Conclusion

We have found that the structural variation of the core units, while retaining the same end-capping units, of small-molecule acceptors has an impact on their optoelectronic structures, molecular ordering, and morphology of their blends with polymer donors and their photovoltaic performance. We fabricated OPV devices using PTQ10 as the donor and four acceptors featuring chlorinated end-capping groups: ID-4Cl, IT-4Cl, m-ITIC-OR-4Cl, and Y7. Changing the core unit affected the domain size of the polymer PTQ10. Y7 featured a ladder-type central fused ring with alkyl chains on the backbone and the nitrogen atoms of the TPBT core unit, replacing the sp^3-hybridized carbon atoms of the IDT and IDTT cores with nitrogen atoms, thereby enhancing the crystallinity of the PTQ10 polymer, allowing it to generate more excitons with better miscibility and a larger interfacial area. The PTQ10:Y7 blend displayed outstanding properties that facilitated more effective charge separation, a broader optical absorption range, and a higher absorption coefficient, all of which were beneficial for greater photon utilization. This blend exhibited a strong ICT, with the resulting PTQ10:Y7-based device achieving the highest PCE (14.5%) among our tested systems. The development of high-performance small-molecule acceptors can thus be concluded to have 1) S, N-heteroarenes ladder-type fused-ring cores with the electron density being distributed along with the lone-pair electron on the nitrogen atom, extending the conjugation, and 2) with the sp^2-hybridized nitrogen side chain, as compared with sp^3-hybridized carbon, that decreases steric hindrance on the small-molecular backbone for facilitating π–π stacking. This strategy of engineering the core unit would appear to be a general one for improving the performance of OPVs.

4. Experimental Section

Materials: The polymer donor poly[thiophene–*alt*–(6,7-difluoro-2-(2-hexyldecyloxy)quinoxaline)] (PTQ10) and Poly[[4,8-bis[5-(2-ethylhexyl)-4-fluoro-2-thienyl]benzo[1,2-b:4,5-b′]dithiophene-2,6-diyl]-2,5-thiophenediyl [5,7-bis(2-ethylhexyl)-4,8-dioxo-4 H,8 H-benzo[1,2-c:4,5-c′]dithiophene-1,3-diyl]-2,5-thiophenediyl] (PM6) were purchased from Derthon and used without further purification.

2,2′-((2Z,2′Z)-((4,4,9,9-Tetrahexyl-4,9-dihydro-*s*-indaceno[1,2-*b*:5,6-*b*′]dithiophene-2,7-diyl)bis(methanylylidene))bis(5,6-dichloro-3-oxo-2,3-dihydro-1*H*-indene-2,1-diylidene))dimalononitrile (ID-4Cl),[37] 3,9-bis(2-methylene-((3-(1,1-dicyanomethylene)-6,7-dichloro)indanone))-5,5,11,11-tetrakis(4-hexylphenyl)dithieno[2,3-*d*:2′,3′-*d*′]-*s*-indaceno[1,2-*b*:5,6-b′]dithiophene (IT-4Cl),[38] 3,9-bis(2-methylene-((3-(1,1-dicyanomethylene)-6,7-dichloro)indanone))-5,5,11,11-tetrakis(3-hexyloxyphenyl)dithieno[2,3-*d*:2′,3′-*d*′]-*s*-indaceno[1,2-*b*:5,6-*b*′]dithiophene (m-ITIC-OR-4Cl),[27a] and 2,2′-((2Z,2′Z)-((12,13-bis(2-ethylhexyl)-3,9-diundecyl-12,13-dihydro-[1,2,5]thiadiazolo[3,4-*e*]thieno[2″,3″:4′,5′]thieno[2′,3′:4,5]pyrrolo[3,2-*g*]thieno[2′,3′:4,5]thieno[3,2-*b*]indole-2,10-diyl)bis(methanylylidene))bis(5,6-dichloro-3-oxo-2,3-dihydro-1*H*-indene-2,1-diylidene))dimalononitrile (Y7)[19b] were prepared according to reported procedures.

Zinc acetate dihydrate [$Zn(CH_3COO)_2{\cdot}2H_2O$] (1.0 g) and ethanolamine (0.28 g) were dissolved in 2-methoxyethanol (10 mL) via vigorous stirring overnight with exposure to the air.

Photovoltaic Devices: Indium tin oxide (ITO)-coated glass substrates were cleaned step wise in detergent, water, acetone, and isopropyl alcohol (ultrasonication, 20 min each) and then dried in an oven for 1 h; the substrates were then treated with UV ozone for 20 min prior to use.

A thin layer (≈ 40 nm) of ZnO was spin coated (4000 rpm) onto the ITO substrates. After annealing at 200 °C for 60 min in air, the substrates were transferred to an N_2-filled glove box. PTQ10 and ID-4Cl (D:A = 1:1.5; 15 mg mL^{-1} in total) were dissolved in chloroform (CF)/1-chloronaphthalene (CN) (100:0.5, v/v); PTQ10 and IT-4Cl (D:A = 1:1.5; 15 mg mL^{-1} in total) were dissolved in CF/CN (100:0.5, v/v); PTQ10 and m-ITIC-OR-4Cl (D:A = 1:1.5; 17 mg mL^{-1} in total) were dissolved in CF/CN (100:0.5, v/v); and PTQ10 and Y7 (D:A = 1:1.5; 22 mg mL^{-1} in total) were dissolved in CF/CN (100:0.5, v/v). PM6 and ID-4Cl (D:A = 1:1.2; 16 mg mL^{-1} in total) were dissolved in chloroform (CF)/1-chloronaphthalene (CN) (100:0.5, v/v); PM6 and IT-4Cl (D:A = 1:1.2; 16 mg mL^{-1} in total) were dissolved in CF/CN (100:0.5, v/v); PM6 and m-ITIC-OR-4Cl (D:A = 1:1.2; 18 mg mL^{-1} in total) were dissolved in CF/CN (100:0.5, v/v); and PM6 and Y7 (D:A = 1:1.2; 21 mg mL^{-1} in total) were dissolved in CF/CN (100:0.5, v/v). Each solution was prepared in a glove box and stirred for 1 h at 60 °C. The solutions were then spin cast on top of the ZnO films. After the CF in the films had evaporated, the films were annealed at 120 °C for 10 min. The active layers of the polymer/small-molecule blends showed thicknesses of ≈110 nm. BHJ devices were fabricated with structures incorporating ITO/ZnO. The devices were ready for measurement after thermal deposition (pressure: ≈ 1×10^{-7} mbar) of a 10 nm-thick film of MoO_3 and then a 100 nm-thick Ag film as the anode. The effective layer area of one cell was 0.1 cm^2. The current density–voltage (*J*–*V*) characteristics were measured using a Keithley 2400 source meter. The photocurrent was measured under simulated AM 1.5 G illumination at 100 mW cm^{-2}, using a Xe lamp-based Newport 66902150 W solar simulator. A calibrated Si photodiode with a KG-5 filter was used to confirm illumination intensity. EQE spectra were measured using an SRF50 system (Optosolar, Germany). A calibrated monosilicon diode exhibiting a response at 300–1000 nm was used as a reference. For measurements of hole and electron mobilities, hole- and electron-only diodes were fabricated having the architectures ITO/poly(3,4-ethylenedioxythiophene):polystyrenesulfonate (PEDOT:PSS)/active layer/gold (Au) and ITO/ZnO/active layer/aluminum (Al), respectively. Mobilities were extracted by fitting the dark *J*–*V* curves into the SCLC model.

Measurements and Characterization: A UV–vis spectrophotometer (Hitachi U-4100) equipped with an integrating sphere was used to acquire absorption spectra. A fluorescence spectrophotometer (Hitachi F-7000 and Fluoromax plus) was used to record the steady-state PL spectra under ambient conditions in air. Film morphologies were determined through the AFM in the tapping mode (Veeco Innova) under ambient conditions. The structures of the small molecules were optimized using DFT (B3LYP/6-31 G**); frequency analysis was conducted to ensure that the optimized structures were stable states. All calculations were carried out using Gaussian 06. Water contact angles were measured using a water contact angle measurement system; surface energies were calculated using the equation of state. The thickness of the active layer of the device was measured using a VeecoDektak 150 surface profiler. GIWAXS and GISAXS analyses (X-ray beam energy: 8 keV [λ = 1.550 Å]; incident angle: 0.2°; sample-to-detector distance: 5 m) over the sampled volume were conducted at the BL23A SWAXS endstation of the National Synchrotron Radiation Research Center (NSRRC), Hsinchu, Taiwan. Cyclic voltammetry (CV) of the polymer films was conducted using a BAS 100 electrochemical analyzer operated at a scan rate of 50 mV s^{-1}; the solvent was anhydrous MeCN, containing 0.1 M tetrabutylammonium hexafluorophosphate ($TBAPF_6$) as the supporting electrolyte. The potentials were measured against a Ag/Ag^+ (0.01 M AgNO3) reference electrode, using the ferrocene/ferrocenium ion (Fc/Fc^+) pair as the internal standard (0.09 V). The onset potentials were determined from the crossing of two tangents drawn at the S-16 increasing and background currents of the cyclic voltammograms. HOMO energy levels were estimated relative to the energy level of the ferrocene reference (4.8 eV below vacuum level).

© 2020 Wiley-VCH GmbH

Supporting Information

Supporting Information is available from the Wiley Online Library or from the author.

Acknowledgements

H-C.W. and C-H.C. contributed equally to this work. H.-C.W., C.-H.C., Y.-C.L., and K.-H.W. thank the Ministry of Education Subsidies for Universities and Tertiary Colleges to Develop International Bilateral Program to Jointly Train World Class Professionals, Taiwan. This study was supported financially by the Center for Emergent Functional Matter Science of National Chiao Tung University from the Featured Areas Research Center Program within the framework of the Higher Education Sprout Project by the Ministry of Education (MOE) in Taiwan, as well as the Ministry of Science and Technology, Taiwan (MOST 107-2923-M-009-004-MY3 and MOST 109-2221-E-009-064-MY3).

Conflict of Interest

The authors declare no conflict of interest.

Keywords

core units, grazing-incidence X-ray scattering, morphologies, organic solar cells, small-molecule acceptors

Received: May 18, 2020
Revised: July 11, 2020
Published online: August 6, 2020

[1] a) H.-W. Cheng, P. Raghunath, K.-I. Wang, P. Cheng, T. Haung, Q. Wu, J. Yuan, Y.-C. Lin, H.-C. Wang, Y. Zou, Z.-K. Wang, M. C. Lin, K.-H. Wei, Y. Yang, *Nano Lett.* **2020**, *20*, 715; b) S. Tan, I. Yavuz, N. De Marco, T. Huang, S.-J. Lee, C. S. Choi, M. Wang, S. Nuryyeva, R. Wang, Y. Zhao, H.-C. Wang, T.-H. Han, B. Dunn, Y. Huang, J.-W. Lee, Y. Yang, *Adv. Mater.* **2020**, *32*, 1906995; c) W. Gao, Q. An, M. Hao, R. Sun, J. Yuan, F. Zhang, W. Ma, J. Min, C. Yang, *Adv. Funct. Mater.* **2020**, *30*, 1908336; d) H. Min, M. Kim, S.-U. Lee, H. Kim, G. Kim, K. Choi, J. H. Lee, S. I. Seok, *Science* **2019**, *366*, 749.

[2] a) R. Wang, J. Yuan, R. Wang, G. Han, T. Huang, W. Huang, J. Xue, H.-C. Wang, C. Zhang, C. Zhu, P. Cheng, D. Meng, Y. Yi, K.-H. Wei, Y. Zou, Y. Yang, *Adv. Mater.* **2019**, *31*, 1904215; b) P. Cheng, G. Li, X. Zhan, Y. Yang, *Nat. Photon.* **2018**, *12*, 131; c) J. Yuan, T. Huang, P. Cheng, Y. Zou, H. Zhang, J. L. Yang, S.-Y. Chang, Z. Zhang, W. Huang, R. Wang, D. Meng, F. Gao, Y. Yang, *Nat. Commun.* **2019**, *10*, 570.

[3] a) X. Du, Y. Yuan, L. Zhou, H. Lin, C. Zheng, J. Luo, Z. Chen, S. Tao, L.-S. Liao, *Adv. Funct. Mater.* **2020**, *30*, 1909837; b) Z. Xing, X. Meng, R. Sun, T. Hu, Z. Huang, J. Min, X. Hu, Y. Chen, *Adv. Funct. Mater. 30*, 202000417; c) Y. Cui, H. Yao, T. Zhang, L. Hong, B. Gao, K. Xian, J. Qin, J. Hou, *Adv. Mater.* **2019**, *31*, 1904512; d) Y. Liu, P. Cheng, T. Li, R. Wang, Y. Li, S.-Y. Chang, Y. Zhu, H.-W. Cheng, K.-H. Wei, X. Zhan, B. Sun, Y. Yang, *ACS Nano* **2019**, *13*, 1071; e) H. S. Ryu, S. Y. Park, T. H. Lee, J. Y. Kim, H. Y. Woo, *Nanoscale* **2020**, *12*, 5792; f) Y. Song, K. Zhang, S. Dong, R. Xia, F. Huang, Y. Cao, *ACS Appl. Mater. Interfaces* **2020**, *12*, 18473.

[4] a) H. W. Cho, N. G. An, S. Y. Park, Y. S. Shin, W. Lee, J. Y. Kim, S. Song, *Adv. Energy Mater.* **2020**, *10*, 1903585; b) Y. Wang, J. Li, T. Li, J. Wang, K. Liu, Q. Jiang, J. Tang, X. Zhan, *Small* **2019**, *15*, 1903977; c) Y.-J. Huang, P.-J. Yen, H.-C. Wang, H.-C. Chen, K.-H. Wei, *Org. Electron.* **2019**, *72*, 6.

[5] Y. Cui, H. Yao, J. Zhang, K. Xian, T. Zhang, L. Hong, Y. Wang, Y. Xu, K. Ma, C. An, C. He, Z. Wei, F. Gao, J. Hou, *Adv. Mater. 32*, 1908205.

[6] a) Y.-W. Su, W.-H. Lin, Y.-J. Hsu, K.-H. Wei, *Small* **2014**, *10*, 4427; b) J.-M. Jiang, M.-C. Yuan, K. Dinakaran, A. Hariharan, K.-H. Wei, *J. Mater. Chem. A* **2013**, *1*, 4415.

[7] X. Ma, J. Wang, Q. An, J. Gao, Z. Hu, C. Xu, X. Zhang, Z. Liu, F. Zhang, *Nano Energy* **2020**, *70*, 104496.

[8] a) Y.-W. Su, Y.-C. Lin, K.-H. Wei, *J. Mater. Chem. A* **2017**, *5*, 24051; b) M.-Y. Chiu, U. S. Jeng, M.-S. Su, K.-H. Wei, *Macromolecules* **2010**, *43*, 428; c) Y. Liu, J. Zhao, Z. Li, C. Mu, W. Ma, H. Hu, K. Jiang, H. Lin, H. Ade, H. Yan, *Nat. Commun.* **2014**, *5*, 5293; d) D. K. Tran, N. B. Kolhe, Y.-J. Hwang, D. Kuzuhara, T. Koganezawa, S. A. Jenekhe, *ACS Appl. Mater. Interfaces* **2020**, *12*, 16490.

[9] a) B. Lu, Z. Chen, B. Jia, J. Wang, W. Ma, J. Lian, P. Zeng, J. Qu, X. Zhan, *ACS Appl. Mater. Interfaces* **2020**, *12*, 14029; b) Y. Zhang, F. Cai, J. Yuan, Q. Wei, L. Zhou, B. Qiu, Y. Hu, Y. Li, H. Peng, Y. Zou, *Phys. Chem. Chem. Phys.* **2020**, *22*, 1787.

[10] a) X. Li, J. Yao, I. Angunawela, C. Sun, L. Xue, A. Liebman-Pelaez, C. Zhu, C. Yang, Z.-G. Zhang, H. Ade, Y. Li, *Adv. Energy Mater.* **2018**, *8*, 1800815; b) C.-H. Chen, Y.-J. Lu, Y.-W. Su, Y.-C. Lin, H.-K. Lin, H.-C. Chen, H.-C. Wang, J.-X. Li, K.-H. Wu, K.-H. Wei, *Org. Electron.* **2019**, *71*, 185.

[11] a) Q. He, M. Shahid, X. Jiao, E. Gann, F. D. Eisner, T. Wu, Z. Fei, T. D. Anthopoulos, C. R. McNeill, M. Heeney, *ACS Appl. Mater. Interfaces* **2020**, *12*, 9555; b) T. J. Aldrich, M. Matta, W. Zhu, S. M. Swick, C. L. Stern, G. C. Schatz, A. Facchetti, F. S. Melkonyan, T. J. Marks, *J. Am. Chem. Soc.* **2019**, *141*, 3274.

[12] a) W. Tang, L. Yang, Z. Hu, Z. Zhang, J. Cao, H. Wang, J. Yu, F. Zhang, *J. Mater. Chem. A* **2020**, *8*, 5458; b) Q. Wang, M. Li, X. Zhang, Y. Qin, J. Wang, J. Zhang, J. Hou, R. A. J. Janssen, Y. Geng, *Macromolecules* **2019**, *52*, 4464.

[13] H. Wang, J. Cao, J. Yu, Z. Zhang, R. Geng, L. Yang, W. Tang, *J. Mater. Chem. A* **2019**, *7*, 4313.

[14] C. Sun, F. Pan, S. Chen, R. Wang, R. Sun, Z. Shang, B. Qiu, J. Min, M. Lv, L. Meng, C. Zhang, M. Xiao, C. Yang, Y. Li, *Adv. Mater.* **2019**, *31*, 1905480.

[15] W. Zhu, J. M. Alzola, T. J. Aldrich, K. L. Kohlstedt, D. Zheng, P. E. Hartnett, N. D. Eastham, W. Huang, G. Wang, R. M. Young, G. C. Schatz, M. R. Wasielewski, A. Facchetti, F. S. Melkonyan, T. J. Marks, *ACS Energy Lett.* **2019**, *4*, 2695.

[16] L. Ye, B. A. Collins, X. Jiao, J. Zhao, H. Yan, H. Ade, *Adv. Energy Mater.* **2018**, *8*, 1703058.

[17] Z.-P. Yu, Z.-X. Liu, F.-X. Chen, R. Qin, T.-K. Lau, J.-L. Yin, X. Kong, X. Lu, M. Shi, C.-Z. Li, H. Chen, *Nat. Commun.* **2019**, *10*, 2152.

[18] Y. Yang, Z.-G. Zhang, H. Bin, S. Chen, L. Gao, L. Xue, C. Yang, Y. Li, *J. Am. Chem. Soc.* **2016**, *138*, 15011.

[19] a) J. Yuan, Y. Zhang, L. Zhou, G. Zhang, H.-L. Yip, T.-K. Lau, X. Lu, C. Zhu, H. Peng, P. A. Johnson, M. Leclerc, Y. Cao, J. Ulanski, Y. Li, Y. Zou, *Joule* **2019**, *3*, 1140. b) Y. Cui, H. Yao, J. Zhang, T. Zhang, Y. Wang, L. Hong, K. Xian, B. Xu, S. Zhang, J. Peng, Z. Wei, F. Gao, J. Hou, *Nat. Commun.* **2019**, *10*, 2515.

[20] T. Xia, C. Li, H. S. Ryu, X. Sun, H. Y. Woo, Y. Sun, *Solar RRL* **2020**, *4*, 2000061.

[21] C. Huang, X. Liao, K. Gao, L. Zuo, F. Lin, X. Shi, C.-Z. Li, H. Liu, X. Li, F. Liu, Y. Chen, H. Chen, A. K. Y. Jen, *Chem. Mater.* **2018**, *30*, 5429.

[22] Z. Yao, X. Liao, K. Gao, F. Lin, X. Xu, X. Shi, L. Zuo, F. Liu, Y. Chen, A. K. Y. Jen, *J. Am. Chem. Soc.* **2018**, *140*, 2054.

[23] a) S. Liu, J. Yuan, W. Deng, M. Luo, Y. Xie, Q. Liang, Y. Zou, Z. He, H. Wu, Y. Cao, *Nat. Photon.* **2020**, *14*, 300; b) M. Azzouzi, T. Kirchartz, J. Nelson, *Trends Chem.* **2019**, *1*, 49.

© 2020 Wiley-VCH GmbH

[24] a) Y.-W. Su, C.-M. Liu, J.-M. Jiang, C.-S. Tsao, H.-C. Cha, U. S. Jeng, H.-L. Chen, K.-H. Wei, *J. Phys. Chem. C* **2015**, *119*, 3408; b) Y.-C. Huang, W.-S. Liu, C.-S. Tsao, L. Wang, *ACS Appl. Mater. Interfaces* **2019**, *11*, 40310.
[25] P. Müller-Buschbaum, *Adv. Mater.* **2014**, *26*, 7692.
[26] E. Walenta, *Acta Polymer.* **1985**, *36*, 296.
[27] a) Y.-C. Lin, Y.-J. Lu, C.-S. Tsao, A. Saeki, J.-X. Li, C.-H. Chen, H.-C. Wang, H.-C. Chen, D. Meng, K.-H. Wu, Y. Yang, K.-H. Wei, *J. Mater. Chem. A* **2019**, *7*, 3072; b) Y.-C. Lin, C.-H. Chen, R.-H. Li, C.-S. Tsao, A. Saeki, H.-C. Wang, B. Chang, L.-Y. Huang, Y. Yang, K.-H. Wei, *ACS Appl. Polym. Mater.* **2020**, *2*, 636.
[28] L. Lu, T. Zheng, Q. Wu, A. M. Schneider, D. Zhao, L. Yu, *Chem. Rev.* **2015**, *115*, 12666.
[29] L. Ye, H. Hu, M. Ghasemi, T. Wang, B. A. Collins, J.-H. Kim, K. Jiang, J. H. Carpenter, H. Li, Z. Li, T. McAfee, J. Zhao, X. Chen, J. L. Y. Lai, T. Ma, J.-L. Bredas, H. Yan, H. Ade, *Nat. Mater.* **2018**, *17*, 253.
[30] X. Liu, B. Xie, C. Duan, Z. Wang, B. Fan, K. Zhang, B. Lin, F. J. M. Colberts, W. Ma, R. A. J. Janssen, F. Huang, Y. Cao, *J. Mater. Chem. A* **2018**, *6*, 395.
[31] a) H.-C. Wang, Y.-C. Lin, C.-H. Chen, C.-H. Huang, B. Chang, Y.-L. Liu, H.-W. Cheng, C.-S. Tsao, K.-H. Wei, *Nanoscale* **2019**, *11*, 17460; b) B. Liu, Y. Wang, P. Chen, X. Zhang, H. Sun, Y. Tang, Q. Liao, J. Huang, H. Wang, H. Meng, X. Guo, *ACS Appl. Mater. Interfaces* **2019**, *11*, 33505.
[32] A. J. Campbell, D. D. C. Bradley, H. Antoniadis, *J. Appl. Phys.* **2001**, *89*, 3343.
[33] J. A. Bartelt, D. Lam, T. M. Burke, S. M. Sweetnam, M. D. McGehee, *Adv. Energy Mater.* **2015**, *5*, 1500577.
[34] M. Stolterfoht, B. Philippa, A. Armin, A. K. Pandey, R. D. White, P. L. Burn, P. Meredith, A. Pivrikas, *Appl. Phys. Lett.* **2014**, *105*, 013302.
[35] F. Bonaccorso, N. Balis, M. M. Stylianakis, M. Savarese, C. Adamo, M. Gemmi, V. Pellegrini, E. Stratakis, E. Kymakis, *Adv. Funct. Mater.* **2015**, *25*, 3870.
[36] a) G. P. Kini, S. J. Jeon, D. K. Moon, *Adv. Mater.* **2020**, *32*, 1906175; b) B. Fan, W. Zhong, X.-F. Jiang, Q. Yin, L. Ying, F. Huang, Y. Cao, *Adv. Energy Mater.* **2017**, *7*, 1602127.
[37] X. Li, H. Meng, F. Shen, D. Su, S. Huo, J. Shan, J. Huang, C. Zhan, *Dyes Pigments* **2019**, *166*, 196.
[38] H. Zhang, H. Yao, J. Hou, J. Zhu, J. Zhang, W. Li, R. Yu, B. Gao, S. Zhang, J. Hou, *Adv. Mater.* **2018**, *30*, 1800613.

© 2020 Wiley-VCH GmbH